Treatment and Resource Recovery

Tuning of Persulfate Activation from Free Radical to Non-Radical Pathway through the Incorporation of Non-Redox Magnesium Oxide

Ali Jawad, Kun Zhan, Haibin Wang, Ajmal Shahzad, Zehua Zeng, Jia Wang, Xinquan Zhou, Habib Ullah, Zhulei Chen, and Zhuqi Chen

Environ. Sci. Technol., **Just Accepted Manuscript** • DOI: 10.1021/acs.est.9b04696 • Publication Date (Web): 23 Jan 2020

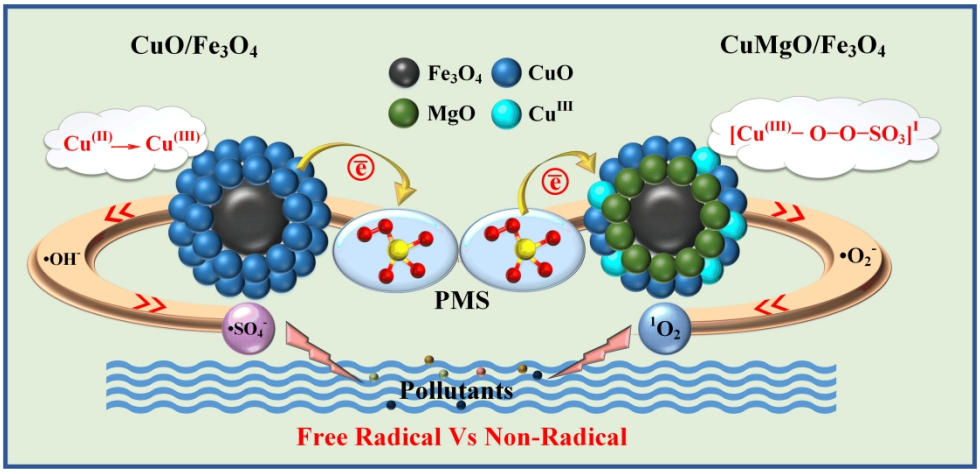

Table of content: The incorporation of MgO tunes the persulfate based oxidation from a classic radical process to a non-radical process

313x145mm (300 x 300 DPI)

Tuning of Persulfate Activation from Free Radical to Non-Radical Pathway through the Incorporation of Non-Redox Magnesium Oxide

Ali Jawad,[1,2] Kun Zhan,[1] Haibin Wang,[2] Ajmal Shahzad,[1] Zehua Zeng,[2] Jia Wang,[1] Xinquan Zhou,[1] Habib Ullah,[3] Zhulei Chen,[1] and Zhuqi Chen,*[2]

[1] Hubei Provincial Engineering Laboratory of Solid Waste Treatment, Disposal and Recycling, School of Environmental Science and Engineering, Huazhong University of Science and Technology, Wuhan 430074, P. R. China

[2] Key Laboratory of Material Chemistry for Energy Conversion and Storage, Ministry of Education; Hubei Key Laboratory of Material Chemistry and Service Failure, School of Chemistry and Chemical Engineering, Huazhong University of Science and Technology, Wuhan 430074, PR China.

[3] Environment and Sustainably Institute (ESI), University of Exeter, Penryn Campus, Penryn, Cornwall TR109FE, United Kingdom.

* Corresponding author

E-mail address: zqchen@hust.edu.cn.

ABSTRACT: Nonradical-based advanced oxidation processes for pollutants removal have attracted much attention due to their inherent advantages. Herein we report that magnesium oxides (MgO) in CuOMgO/Fe_3O_4 not only enhanced the catalytic properties but also switched the free radical peroxymonosulfate-activated process into the $^1O_2$ based nonradical process. CuOMgO/Fe_3O_4 catalyst exhibited consistent performance in a wide pH range from 5.0 to 10.0, and the degradation kinetics were not inhibited by the common free radical scavengers, anions or natural organic matter. Quantitative structure activity relationships (QSARs) revealed the relationship between the degradation rate constant of 14 substituted phenols and their conventional descriptor variables (i.e. Hammett constants σ, σ^-, σ^+), half-wave oxidation potential ($E_{1/2}$) and pK_a values. QSARs together with kinetic isotopic effect (KIE) recognized the electron transfer as the dominant oxidation process. Characterizations and DFT calculation indicated that the incorporated MgO alters the copper sites to highly oxidized metals centers, offering a more suitable platform for PMS to generate metastable copper intermediates. This highly oxidized metals centers of copper played the key role in producing $O_2^{\bullet-}$ after accepting electron from another PMS molecule, and finally $^1O_2$ as sole reactive species was generated from the direct oxidation of $O_2^{\bullet-}$ through thermodynamically feasible reactions.

KEYWORDS: PMS, nonredox metals, singlet oxygen, nonradical, organic contaminants

Introduction

The worldwide water and soil pollution demanded strongly to develop an effective remediation technology. Recently, chemical oxidation based on peroxymonosulfate (PMS) or peroxydisulfate (PDS) activation has attracted many research groups owing to the generation of powerful hydroxyl (•OH), sulfate ($SO_4^{\bullet-}$) or both radicals.[1–5] Various strategies such as light, heat, ultrasound, electricity and transition metals can be adopted to generate these radicals during the activation of persulfate.[1–10] Among various strategies, transition metals (Co^{2+}, Fe^{2+}, Cu^{2+}, Mn^{2+}), their oxides (Co_3O_4, Fe_3O_4, CuO, MnO_2) and bimetallic composites ($CuFe_2O_4$, CuO-Fe_3O_4, $Mn_{1.8}Fe_{1.2}O_4$ etc.) were recognized as the most efficient approaches.[4-11] In addition, the persulfate activation through a similar pathway can also be achieved using biochar, reduced graphene oxides, carbon nanotubes and N-doped graphene.[12–15]

The effectiveness of advance oxidation systems (H_2O_2/PMS/PS) relies on the strong oxidizing power of free radicals (hydroxyl •OH E^0 1.9−2.7 V and sulfate $SO_4^{\bullet-}$ E^0 2.5–3.1 V) towards a broad spectrum of recalcitrant pollutants.[12-17] However, it can cause undesirable catalytic durability due to its high reactivity for both the target compounds and competing organic/inorganic constituents of water.[18-20]Meanwhile, the difficulty in the regeneration of actives sites due to the energetically unfavorable redox cycles is also considered one of the major drawback in their practical application.

Alternately, the recently discovered non-radical oxidative pathway is highly selective for electron rich organic pollutants, which can reduce the amount of side products.[21-23]The non-radical process requires small amount of oxidants, and the degradation kinetics were less influenced by the competing organic/inorganic constituents or radical scavengers.[22]Non-radicals oxidative pathway can be broadly categorized into surface activated complex, electron transfer mediation and singlet oxygen. The surface activated complex is resulted from the

activation of persulfates at the surface of catalysts and is considered completely different from the free radical oxidation. For example, copper oxides were reported to generate surface metastable complex during the activation of PDS,[21] where the degradation kinetic of 2,4-dichlorophenol was unaffected by excess amounts of Cl^- ions or radical scavengers. Similarly, Pd-Al_2O_3 catalyst mediated electron transfer from organics to PMS, and such persulfate driven activation exhibited a substrate selectivity which was similar to the carbon nano-tube/PMS system.[22-23] In contrast, a substrate selective surface-bound $SO_4^{\bullet-}$ radical mechanism was proposed for Pd-Al_2O_3/PMS system, where the degradation kinetic of 1,4-dioxane was strongly scavenged by radicals scavengers.[24] Contradicting to these reports, certain recent studies have reported the presence of singlet oxygen ($^1O_2$) as another type of nonradical process.[25−32] The $^1O_2$-based pathway is also popular for their resistance to popular scavengers and background substances in water matrix.

Using metal oxides, we recognized that there is a great deal of uncertainty regarding the identification of reactive species. For example, CuO alone or its composite with the oxides of other metals is reported to produce $\bullet SO_4^-$, •OH, surface bound complex or singlet oxygen during persulfate activation.[8,21,29,33] Similar kind of uncertainty also exist for the oxides of other metals,[22,23,26,31-32,34] reflecting that the mechanism behind the identification of reactive species is ambiguous which needs further explorations. Most importantly, it is unclear that how the reaction pathway changes, how non-radical $^1O_2$-PMS activation dominate and how it contributes in the degradation process yet to be answered.

In this work, we surprisingly found that the incorporation of magnesium oxides (MgO) onto typical CuO/Fe_3O_4 catalyst not only enhanced the catalytic properties, but also switched the free radical peroxymonosulfate-activated process into the $^1O_2$ based nonradical process. There is an urgent need to explain not only the positive aspects of MgO in catalysis but also disclose the deeper insight behind the $^1O_2$-based nonradical activation of PMS. Based on various

spectroscopic evidences and DFT calculations, the switching of reaction mechanism was related to the transfer of Cu ions into highly electron deficient state and presence of extensive surface OH groups after the incorporation of MgO. Furthermore, chemical scavenger tests, EPR observation, the solvent dependency, FFA degradation as $^1O_2$-indicator, pH studies, complexation behaviors and the comparison with Rose Bengal (RB), a well-known $^1O_2$-photo sensitize system,[35] were conducted to address the knowledge gap in the identification and generation mechanism of $^1O_2$ in CuOMgO/Fe_3O_4+PMS system. The linear free energy relationships (LFERs) between the degradation rate constants of 14 substituted phenols and conventional descriptor variables (i.e. Hammett constant σ, σ^-, σ^+), quantitative structure activity relationship (QSARs) and kinetic isotopic effect (KIE) revealed the electron transfer between the organic substrate in singlet oxygen dominated process.

Materials and Methods

Materials Preparation

Copper and magnesium oxides were deposited on the surface of Fe_3O_4 by a simple coprecipitation method. First, 100 mL $Mg(NO_3)_2{\cdot}6H_2O$ and $Cu(NO_3)_2{\cdot}6H_2O$ mixed solution in different compositions (Table S1) were drop wisely added to 0.4 M (100 mL) Na_2CO_3 aqueous solution containing 0.5 g of Fe_3O_4 (fixed amount), maintained at 60 °C over a time of 3 hours (h). The prepared catalysts were dried at 80 °C, calcined at 500 °C for 5 h and named as shown in Table S1. For the purpose of comparison, other catalysts CuO, Fe_3O_4, Co_3O_4, MnO_2, their composite with Fe_3O_4 (i.e. CuO/Fe_3O_4, Co_3O_4/Fe_3O_4, MnO_2/Fe_3O_4), MgO incorporated catalysts (i.e. Co_3O_4MgO/Fe_3O_4, MnO_2MgO/Fe_3O_4) or replacing MgO with the oxides of other divalent metals (i.e. CuOCaO/Fe_3O_4, CuOBaO/Fe_3O_4, CuOZnO/Fe_3O_4) or transition metal (CuOCo_3O_4/Fe_3O_4) and replacing Fe_3O_4 with other support (i.e. CuOMgO/Al_2O_3 and CuOMgO/SiO_2) were also prepared using the method mentioned earlier.

Procedure for Pollutant Degradation

The degradation of various organic compounds (O.Cs) was conducted in 30 mL glass bottles under magnetic stirring. Different parameters such as the initial reaction pH, typical background water constituents i.e. Cl^-, NO_3^-, SO_4^{2-}, CO_3^{2-}, HCO_3^-, HPO_4^-, humic acid (HA), kinetics of OCs degradation, decomposition of PMS, oxidation products, recyclability, leaching of active sites, toxicity based on the generation of BrO_3^-, structure activity relationship by considering the degradation of 14 substituted phenolic compounds and kinetic isotopic effect (KIE) were evaluated. Reactions were initiated at uncontrolled initial pH after adding PMS, catalyst and 4-chlorophenol (4-CP) or other substituted OCs in desired concentration with or without a constituent of interest (Cl^-, NO_3^-, SO_4^{-2}, CO_3^{-2}, HCO_3^-, HPO_4^- and HA). Periodically, 1 mL sample was withdrawn, filtered with a 0.2 μM filter (polytetrafluoroethylene syringe filters) and quenched immediately with excess ethanol before analyzing on HPLC. To evaluate the consistent performance at wide effective pH, Rose Bengal (RB) as typical $^1O_2$-generator was also applied for the degradation of 4-CP.[35] The photosensitized process was conducted in 100 mL quartz reactor at different initial pH, using 0.2 mM of RB and light intensity of 280 mW/cm^2. The generation of toxic BrO_3^- as byproduct in brominated medium was analyzed by an ion chromatographic method as reported previously.[36] The zero point charge of catalysts were determined by zeta potential method. To analyse the degradation products of 4-CP on GC-MS, the reaction solution was dried first in freeze drier. The resulted residue was transferred into 10 mL ethyl acetate and then passed through a sodium sulfate packed column to remove the traces of water. The eluent was then concentrated under Ar stream. To derivatized the degradation product, 0.1 mL MSTFA (a derivatizing agent) was added and then followed by heating at 80 ^{o}C for 30 min. Similarly, the PMS concentration after reaction was determined by UV-visible spectrometer as reported previously.[37] In general procedure, 100 μL from sample or standard solutions were added into10 mL mixed solution of

$KHCO_3$ and KI (1.25 g $KHCO_3$ + 10 g KI dissolved in 250 mL deionized water). The subsequent solution were initially hand shake and then analysed on UV-visible spectrometer at 352 nm after reacting for 15 min.

To detect the reactive oxygen species (ROS), chemical scavengers like ethanol, tertiary butyl alcohol (TBA), benzoquinone (BQ), sodium azide (NaN_3) and furfural alcohol (FFA) were applied. To confirm the findings of chemical scavengers, electron paramagnetic resonance (EPR) spectroscopy with spin trapping reagents such as 2,2,6,6-tetramethyl-4-piperidone (TEMP) and 5,5-dimethyl-pyrroline-oxide (DMPO) were applied both in water and ethanol. Additionally, singlet oxygen as sole reactive species was further confirmed after considering FFA degradation, exchanging H_2O with D_2O and detection of H_2O_2. The redox properties of the $CuOMgO/Fe_3O_4$ and CuO/Fe_3O_4 catalysts were determined by the hydrogen temperature programmed reduction method (H_2−TPR).[38–39] Initially, the solid $CuOMgO/Fe_3O_4$ and CuO/Fe_3O_4 catalysts were heated to 350 °C in a quartz reactor under an N_2 flow for 1 h. After cooling the samples to room temperature, the catalysts were reheated to 350 °C (10°/min) in the presence of a reducing agent (10% N_2/H_2 mixture), and the H_2 consumption was calculated (denoted X in Eq. 1). After cooling the catalyst to 50 °C, the surface copper was reoxidized for 0.5 h in the presence of 20% N_2O/N_2. Finally, the second H_2 consumption was determined as described in the same way as the first H_2-TPR (denoted Y in Eq. 2).

$$CuO + H_2 \rightarrow Cu + H_2O \qquad \text{Hydrogen consumption (X)} \qquad (1)$$

$$Cu_2O + H_2 \rightarrow 2Cu + H_2O \qquad \text{Hydrogen consumption (Y)} \qquad (2)$$

The exposed CuO_X surface area (S) and density of surface-active copper sites (D) (Table S2) were calculated as: (Eqs. 3, 4)

$$S = 2 \times Y \times N_{av}/(X \times M_{Cu} \times 1.4 \times 10^{19}) \qquad (3)$$

$$D = (2 \times Y/X) \times 100 \qquad (4)$$

where N_{av}= Avogadro's number, M_{Cu}= the relative atomic mass, and 1.4×10^{19} represents the number of copper atoms per square meter.

DFT Calculations

Quantum-ATK along with VESTA and Virtual NanoLab Version 2019.3 software was employed for the electronic properties simulations of CuO, MgO, Fe_3O_4, CuO/MgO, and CuO/MgO/Fe_3O_4. Density functional theory (DFT) was used for the electronic property's simulations and the detail procedure was given as text S6.

Results and Discussion

PMS Activation by Different Catalysts

The catalytic performance of CuOMgO/Fe_3O_4 along with different controlled catalysts i.e. CuO, Fe_3O_4, MgO, MgO/Fe_3O_4, CuO/Fe_3O_4 and CuOMgO is evaluated during the degradation of 4-CP using PMS activated system (Figure 1A and and Figure S1). As shown, the catalytic performance of various controlled catalysts i.e. MgO, Fe_3O_4, MgO/Fe_3O_4 and CuO or a physical mixture of CuO plus Fe_3O_4 is very poor as revealed from less than 10-30% of 4-CP removal. In the case of bimetallic CuO/Fe_3O_4 catalyst, the removal efficiency was slightly improved to 42%. More interestingly, the degradation of 4-CP reached to 100% with the degradation rate of 0.14-0.16 min^{-1} for CuOMgO or CuOMgO/Fe_3O_4 catalysts, 16 to 50 times higher than CuO/Fe_3O_4 (0.01 min^{-1}), CuO (0.008 min^{-1}) or Fe_3O_4 (0.003 min^{-1}). Additionally, the negligible removal efficiency while using CuOMgO/Fe_3O_4 as adsorbent or homogeneous activation (~100 times to the leached amount of Cu^{2+} and Fe^{2+}) demonstrated the important role of heterogeneous PMS activation. Furthermore, the very poor performance of various catalysts i.e. Fe_3O_4, CuO, CuO/Fe_3O_4 or MgO/Fe_3O_4 clearly revealed that the enhanced catalytic activity of CuOMgO or CuOMgO/Fe_3O_4 was resulted from the increase reactivity of only copper after the incorporation of MgO whereas Fe_3O_4 can only function as support

material, offering the easy recovery of catalyst during reusing. By considering these interesting results, it was necessary to explore the role of MgO more deeply. We therefore, replaced MgO in CuO/Fe_3O_4 catalyst with the oxides of other divalent metals. As shown in Figure S2, the catalytic activity was gradually decreased after replacing MgO with CaO or BaO. This decrease might be related to the large ionic size of Ca^{2+} or Ba^{2+}, influencing the crystal structure of catalyst. As shown (Figure S3 and Table S3), the XRD peaks corresponded to the crystal planes of pure CuO shifted significantly toward the low 2Θ after replacing MgO with CaO or BaO. These results thus suggested that the changes in the catalytic activity of CuO in CuO/Fe_3O_4 catalyst is related to the structural changes. The structural changes in CuO might be more interesting as the incorporation of Zn^{2+} with ionic radii close to Mg^{2+} (Mg^{2+}=0.065 nm, Zn^{2+}= 0.074 nm), also leads to good catalytic activity, showing positive influence the activity of CuO.

We further considered the PMS decomposition efficiency to evaluate the role of MgO in $CuOMgO/Fe_3O_4$. As shown in Figure 1B, both Fe_3O_4 and MgO/Fe_3O_4 were involved in less than 10% PMS decomposition. In contrast, the PMS decomposition gradually increased from CuO to CuO/Fe_3O_4 and finally reached 100% in the case of CuOMgO and $CuOMgO/Fe_3O_4$. These results are in accordance with the catalytic activity order and support strongly that the enhanced catalytic activity was related to the changes in the catalytic activities of copper after the incorporation of MgO. By considering these interesting results, we choose the influence of MgO on the reactivity of other redox metals such as Co and Mn. As shown in Figure 1C and Figure S1, the catalyst such as Co_3O_4MgO/Fe_3O_4 showed significant improvement with 4-CP degradation rate ($k=0.027\ min^{-1}$), higher than Co_3O_4/Fe_3O_4 ($k=0.013\ min^{-1}$) or Co_3O_4 ($k=0.009\ min^{-1}$). A similar pattern of increase was observed for MnO_2MgO/Fe_3O_4 ($k=0.022\ min^{-1}$), highlighting the positive influence of MgO on the catalytic activities of redox metals. More interestingly, the remarkable improvement in the catalytic activity of $CuOMgO/Fe_3O_4$ emphasized maximum influence of MgO on the reactivity of studied redox metals. Additionally,

the influence of support material (Figure 1C and Figure S1) indicate the highest degradation rate (k=0.19 min^{-1}) for $CuOMgO/SiO_2$, followed by $CuOMgO/Fe_3O_4$ (k=0.16 min^{-1}) and $CuOMgO/Al_2O_3$ (k=0.028 min^{-1}). The easy recovery owing to the magnetic property gives extra advantage to $CuOMgO/Fe_3O_4$ for real application and thus was chosen for detail studies.

Changes in the Redox Properties of Copper after the Incorporating MgO

The above results clearly revealed that the incorporated MgO play important role to modify the activity of different Cu-supported catalysts. We believed that this improvement is originated from the significant changes in the catalytic properties of CuO. First, the structural changes observed after replacing MgO with the oxides of other divalent metals (Figure S3 and Table S3) highlighted the structure-activity relationship of CuO. More precisely, the changes in the crystal structural of CuO might be important as the incorporation of ZnO in CuO/Fe_3O_4 catalyst with ionic radii close to Mg^{2+} and Cu^{2+} (Mg^{2+}=0.72 Å, Zn^{2+}= 0.74 Å and Cu^{2+}= 0.73 Å), also leads to good catalytic activity. Additionally, the incorporation of MgO was accounted to increase the surface area (Table S2) and thus correspondingly increase the fine dispersion of active sites. In order to correlate the enhanced catalytic with surface area, normalized rate constants were calculated (Figure S4). The results revealed that the increase of surface area after the incorporation of MgO might not be very important in the enhanced activity of copper due the big difference in the normalized rate constants of $CuOMgO/Fe_3O_4$ (0.02 L m^{-2} min^{-1}) and CuO/Fe_3O_4 (0.004 L m^{-2} min^{-1}). In contrast, these results highlighted that the enhanced activity was related to the increased reactivity of copper as active site after the incorporation of MgO.

Analyzing solid CuO/Fe_3O_4 and $CuOMgO/Fe_3O_4$ catalysts on XPS, H_2-TPR and Raman spectroscopy gave us a solid evidence for the enhanced catalytic activity after the incorporation of MgO. For example as shown in Figure S5, the incorporation of MgO in $CuOMgO/Fe_3O_4$

232 shifted the Cu 2p core spectra toward the high binding energy (B.E 0.88 V), facilitating the
233 generation of Cu ions in highly electron deficient state, most probably be Cu^{3+} species, which
234 offered the highest redox potential for PMS activation (E_o $Cu^{(III)}/Cu^{(II)}$ 2.3 V vs $HSO_5^-/•SO_4^-$
235 1.8 V).[8–10] The H_2−TPR analysis (Figure S6) showed two-stage desorption processes for the
236 CuOMgO/Fe_3O_4: one reduction peak at 157 °C followed by another one at 254 °C, which were
237 attributed to the reductions of Cu species ($Cu^{3+} \rightarrow Cu^{2+}$ and $Cu^{2+} \rightarrow Cu^{+1}$).[38,40] In contrast, the
238 intense reduction peaks of the CuO/Fe_3O_4 were shifted to much higher temperatures (218 and
239 345 °C), indicating that the Cu species in the CuO/Fe_3O_4 catalyst were less electron deficient
240 as compared to CuOMgO/Fe_3O_4. Moreover, calculated from the chemical adsorption volume
241 of H_2, the %CuO_x dispersion and exposed CuO_x active surface area was 16.62% and 112.40
242 m^2/g, respectively, for the CuOMgO/Fe_3O_4, both of which were obviously higher than
243 CuO@Fe_3O_4 (12.53% and 84.79 m^2/g, respectively), (Table S2). Raman spectroscopy was
244 applied to confirm the evidence of XPS and H_2-TPR analysis. As shown in Figure 1D, the
245 characteristics Raman peaks corresponded to Fe_3O_4 and CuO were broader for both CuO/Fe_3O_4
246 and CuOMgO/Fe_3O_4 catalysts. However, the shifting in the latter case was more obvious,
247 indicating the abundant lattice defects and more reactive active sites.[41] More interestingly, the
248 marker peak of Cu^{3+} state at 603 cm^{-1} as reported in the characteristic Raman spectrum of
249 $NaCuO_2$ was only observed in CuOMgO/Fe_3O_4 catalyst.[42] This result give us another solid
250 evidence for the existence of Cu^{3+} state, and thus confirmed the findings of XPS and H_2-TPR
251 analysis.

252 To clarify the role of MgO in the generation of Cu^{3+} state, we performed a series of DFT
253 calculations to simulate the partial density of states (PDOS), band structure simulation and
254 Bader charge transfer analysis of CuO, Fe_3O_4, CuOMgO and CuOMgO/Fe_3O_4. The detail
255 simulation procedure is given in the supporting information as Text S6. First, partial density of
256 states (PDOS) simulation were applied to investigate the changes in the electronic states, after

the incorporation of MgO (Figure S7). In the case of CuO/Fe_3O_4 system (Figure S7 A), Cu has the highest density of states in the valence band (VB) while the conduction band (CB) is equally contributed by the anti-bonding orbitals of O, Fe, and Cu atoms. On the other hand, the density of states of Cu in the VB of $CuOMgO/Fe_3O_4$ is comparatively reduced while its density is increased in the CB (Figure 7S B). In addition, the Fermi energy level of CuO/Fe_3O_4 has also been increased from -5.33 to -5.37 eV, upon MgO incorporation. In order to further clarify this effect, the density of states for valence and conduction bands of $CuOMgO/Fe_3O_4$ were plotted separately (Figure S8). Comprehensive analysis of Figure S8 and the spin-up down PDOS spectra of $CuOMgO/Fe_3O_4$ (Figures S9), clearly suggested that the density of states of Cu in the CB of $CuOMgO/Fe_3O_4$ increases, due to the oxidation of some of the Cu atoms i.e., from Cu^{2+} to Cu^{3+}. Furthermore, the comparative analysis of band structure of CuO/Fe_3O_4 and $CuOMgO/Fe_3O_4$ (Figures S10-S12) let us to conclude that MgO has produced an extra band within the bandgap of parent CuO/Fe_3O_4, responsible for the bandgap reduction and trapping centre of extra charge (Cu^{3+}). This band arises from the anti-bonding orbital of Mg in the spin-up state only, while it is fully hybridized with anti-bonding orbitals of Fe, Cu and O atoms, as can be seen from Figure S11 and S12. Therefore, the changes in density of state of VB and CB after the incorporation of MgO is responsible for the generation of Cu^{3+} state as also evident from Bader charge analysis. The results of Figure S13 and Table S4, suggested that Cu has +2 charge in CuO while its valency increases from Cu^{2+} to Cu^{3+}, upon interaction of MgO either in the case of CuOMgO or $CuOMgO/Fe_3O_4$. For example, Cu donates about ~1.54 electrons to O which form Cu^{2+} state in the case of CuO/Fe_3O_4 (Figure S13 A). On the other hand, Cu donates about ~2.65 electrons (equivalent to Cu^{3+} state) and thus enhanced the performance of both CuO/MgO and $CuOMgO/Fe_3O_4$ heterostructure due to the presence of Cu in high oxidation state.

Identification of Reactive Oxygen Species

Sulfate ($SO_4^{\bullet-}$) and hydroxyl (•OH) radicals have been reported as the dominant reactive species in PMS activated systems.[21-24] Firstly, tertiary butyl alcohol (TBA) and ethanol were applied in excess amount (1000 fold) as selective radical scavengers for •OH and $SO_4^{\bullet-}$ radicals because of their dissimilar second-order rate constants. For example, TBA react quickly with •OH radicals (k_2 (TBA, •OH = 3.6–7.6 × 10^9 M^{-1}s-1), over 1000 fold faster than $SO_4^{\bullet-}$ (k_2 (TBA, $SO_4^{\bullet-}$ = 4–9.1 × 10^5 $M^{-1}s^{-1}$). Similarly, ethanol react both •OH and $SO_4^{\bullet-}$ radicals nearly with the same rate i.e. k_2 (ethanol, •OH = 1.1–2.8 × 10^9 $M^{-1}s^{-1}$) and k_2 (ethanol, $SO_4^{\bullet-}$ = 1.6–7.8 × 10^7 $M^{-1}s^{-1}$) and thus can used to trap both radicals.[7] As shown in Figure 2A and Figure S14, the inhibitory effect of both these scavengers were negligible for CuOMgO/Fe_3O_4+PMS system as k_{obs} only changes from 0.162 min^{-1} to 0.150 min^{-1} or 0.152 min^{-1} after applying excess amount of ethanol or TBA. In contrast, the degradation rate of 4-CP in the CuO/Fe_3O_4+PMS system decreased from 0.01 min^{-1} to 0.008 min^{-1} in the presence of ethanol and to 0.004 min^{-1} in the presence of TBA (Figure S15). Similarly, for the CuO+PMS system, the degradation rate of 4-CP was also influenced by both ethanol and TBA (Figure S16). These results thus highlighted that the incorporated MgO as CuOMgO/Fe_3O_4 play important role to switch the degradation pathway from radical to non-radical process. To further confirm these results, we performed the scavenging studies on CuOCaO/Fe_3O_4 and CuOZnO/Fe_3O_4 catalysts where MgO was replaced with the oxides of other divalent metals. As shown in Figure S17, the degradation of 4-CP was not inhibited in both CuOCaO/Fe_3O_4+PMS and CuOZnO/Fe_3O_4+PMS system after applying excess amount of radical scavengers and thus indicated the presence of reactive species similar like CuOMgO/Fe_3O_4+PMS system. In contrast, the degradation was inhibited significantly in the case of $CuOCo_3O_4$/Fe_3O_4+PMS system where MgO was replaced with the oxide of transition metals. These results thus strongly verify the major role of MgO to change the reaction mechanism from radical to non-radical.

306 Moreover, we applied sodium azide (NaN_3) at different concentrations (inset of Figure 2A and
307 Figure S18) to quench the singlet oxygen (k_2 $^1O_2$= 1× 10^9 $M^{-1}s^{-1}$).[26-30] As shown, the
308 degradation of 4-CP was almost suspended in CuOMgO/Fe_3O_4+PMS system in the presence
309 of 50-100 mM NaN_3. For example, almost 90% inhibition with a decrease in the degradation
310 rate from the initial 0.16 min^{-1} to 0.006 min^{-1} was noted after adding 100 mM NaN_3. In contrast,
311 the degradation rate of 4-CP in the presence of CuO/Fe_3O_4+PMS was barely affected (Figure
312 S19). These results thus suggested the dominant role of $^1O_2$ in CuOMgO/Fe_3O_4+PMS system.
313 To validate the leading role of $^1O_2$, the degradation of FFA as $^1O_2$-indicator was performed
314 (Figure 2B and Figure S20).[43] As shown, the removal of FFA through adsorption or PMS alone
315 was negligible, however the removal was more rapid when the catalyst and PMS were applied
316 together and almost all FFA (0.1-10 mM) was completely removed in different reaction time.
317 The first order degradation rate constant of FFA, calculated at 0.1 mM was 0.3085 min^{-1}, which
318 was far higher than that of 4-CP (0.16 min^{-1}). Moreover, the calculated amount of $^1O_2$ from the
319 degradation of FFA, using the equation of $[^1O_2]= k_{obs}/FFA$, was 1.848 × 10^{-4} M (at 10.0 mM
320 FFA) (Figure S20), which was much higher than MnO_2/PDS system (1.65 × 10^{-11} M at 0.3
321 mM FFA)[26] and typical $^1O_2$-mediated RB light irradiated system (0.05 × 10^{-11} M at 0.27 mM
322 FFA).[35] To further confirmed the presence of $^1O_2$ as dominant reactive species, the degradation
323 of 4-CP was conducted in D_2O. As shown in Figure S21, the kinetic degradation of 4-CP was
324 significantly increased after exchanging H_2O with D_2O. This improvement was related to the
325 enhanced stability of $^1O_2$ (10 times) in D_2O and thus gives strong evidence for the generation
326 of singlet oxygen.[43] To endorse the results of the chemical scavengers, electron paramagnetic
327 resonance was also applied. The typical three-line spectrum (1: 1: 1) with TEMP (Figure 2C),
328 confirmed the presence of $^1O_2$ in the CuOMgO/Fe_3O_4+PMS system. In addition, the intensities
329 of the three-line spectra decreased after adding NaN_3 (5 mM) or FFA (0.1 mM) due to the
330 scavenging of singlet oxygen. In contrast, no signals were observed for •OH or SO_4^{-}• after

adding DMPO (Figure S22) in water. These results thus verified that the degradation process in CuOMgO/Fe_3O_4+PMS system was dominantly controlled by $^1O_2$ oxidation process.

Interactions between Catalyst and PMS

Previously we compared the decomposition of PMS between Fe_3O_4, MgO/Fe_3O_4, CuOMgO and CuOMgO/Fe_3O_4 to demonstrate the reactivity originated from CuO rather than from Fe_3O_4 (Figure 2B). Herein, we conducted additional experiments to see how the decomposition of PMS was influenced by the addition of 4-CP to further investigate the interactions between catalysts and PMS (Figure 1B and Figure S23). As shown, the presence of both catalysts without organic decomposed PMS to significant extent. However, the decomposition of PMS was 13 times faster for CuOMgO/Fe_3O_4 as compared to CuO/Fe_3O_4. The faster PMS decomposition was related to Cu^{3+} state, as revealed above, offering thermodynamically feasible sites to accept electron from PMS (E_o $Cu^{(III)}/Cu^{(II)}$ 2.3 V vs. E^o HSO_5^-/SO_4^{2-} 1.81 V). This was further evidenced from the gradual increase in the reduction peaks of CuOMgO/Fe_3O_4 after applying increasing amount of PMS (Figure 2D), and thus highlighted the reverse phenomena from the early reports.[22,44–45] Additionally, the decrease of PMS decomposition after 4-CP addition (Figure S23) ruled out the mediator role of catalyst as proposed in the early reports,[22,44-45] through which the direct electron transfer between organic contaminants and PMS was considered as the dominant process. Additionally, the improved charge transfer ability of CuOMgO/Fe_3O_4 by EIS and CV studies (Figure S24) further demonstrated that Cu^{3+} state could accept electron more quickly from PMS, and thus induce faster PMS decomposition.

Another property is the type of complexation (inner-sphere vs. outer-sphere) of PMS to decide the nature of dominant mechanism.[7,21] Therefore, we studied the complexation behavior of PMS at the surface of CuOMgO/Fe_3O_4 and CuO/Fe_3O_4 at increasing ionic strength (taken as 1−100 mM $NaClO_4$). In the case of CuOMgO/Fe_3O_4, the degradation of 4-CP was significantly

influenced at increasing ionic strength (Figure S25). This relationship revealed that the interaction between the CuOMgO/Fe_3O_4 and PMS occurred through the outer-sphere surface complexation because the increasing ionic strength inhibited the electrostatic interactions between the PMS molecules and catalyst particles. In contrast, the degradation of 4-CP was not influenced for CuO/Fe_3O_4 at increasing ionic strength due to presence of the inner-sphere complexation (covalent or ionic bonding) between the catalyst particles and PMS molecules (Figure S26).[7,21] ATR-FTIR spectra was further applied to visualize the inner-sphere complexation of S−O bond coming from the PMS in the range of 1249−1060 cm^{-1}.[21] As shown (Figure 3A), we obtained the evidence of bonding PMS at the surface of catalyst in the IR range of 1101−1097 cm^{-1} for radical dominant systems (CuO/PMS or CuO/Fe_3O_4/PMS). In contrast, the absence of IR peaks in the above range confirmed the lack of inner-sphere complexation between PMS and CuOMgO/Fe_3O_4 catalyst.

The changes in the complexation was interesting to decide the difference between radical and non-radical oxidation process. Surface hydroxyl group is documented in many recent publication and is believed to play important role in the catalytic activity of catalysts.[46-49] Therefore, we expected that the changes in the surface hydroxyl groups after the incorporation of MgO might be important to change the PMS complexation from inner sphere to outer sphere. Therefore, we compared the proportion of surface hydroxyl groups on CuOMgO/Fe_3O_4, CuO/Fe_3O_4 and CuO and Fe_3O_4 catalysts (Figure S27). Based on the XPS peak area (Figure S27), the proportion of terminal-OH, bridging-OH and oxides (50: 36: 14) at the surface of CuOMgO/Fe_3O_4 was much higher than the dominant radical based catalysts i.e. CuO/Fe_3O_4, CuO and Fe_3O_4.[46]Additionally, the XPS results were further verified through FTIR analysis (Figure S28). As shown, the incorporation of MgO as CuOMgO or CuOMgO/Fe_3O_4 visibly increased the intensity of peak corresponded to terminal-OH and bridging-OH groups.[50,51] Even though, all oxides are hydroxylated due to the chemisorption of water, however, the

increase of hydroxyl groups (terminal-OH and bridging-OH) at the surface of CuOMgO/Fe_3O_4 after the incorporation of MgO is not surprising because MgO is strongly basic with high isoelectric point of 11.80.[52]Thus it is inferred that the densely OH covered surface of CuOMgO/Fe_3O_4 might provide strong binding sites for PMS through H-bonding,[50,51] leading to strong electrostatic interactions and changes the complexation behaviour of PMS from inner sphere to outer sphere. Furthermore, the DFT calculations also clarified that the OH groups on the surface of CuOMgO/Fe_3O_4 catalyst are more strongly bonded (bond length 1.99 Å) as compared to CuO/Fe_3O_4 (2.28 Å), showing adsorption energy (-1563.27 kcal/mol Table S5), eight times higher (202.01 kcal/mol) than CuO/Fe_3O_4 (Figure S29 and S30). The shorter bond length and high adsorption energy in the case of CuOMgO/Fe_3O_4 catalyst might related to the existence of strong H-bonding between the surface OH groups,[51,52] and thus supporting indirectly the existence of strong electrostatic interactions between PMS and catalyst particle. Since, HPO_4^- offer strong affinity to replace the surface OH groups of catalyst and interact directly the active sites through inner sphere complexation.[53] Therefore, it is expected that the application of H_2PO_4 during 4-CP degradation would disturb the H-bonding interactions of PMS and surface OH groups. As shown (Figure S31), the significant influence on 4-CP degradation in the presence of H_2PO_4 is related to the unavailability of surface hydroxyl groups to interact PMS and thus gives direct evidence for the importance of surface OH groups. These results thus gives us enough evidences to support the switching of PMS complexation from inner-sphere to outer-sphere was related to the presence of extensive surface hydroxyl groups after MgO incorporation, responsible for generating different reactive species.

Proposed Mechanism for the Generation of $^1O_2$

The generation of singlet oxygen can be achieved by many pathways including the reaction between PMS/PDS and kenotic groups in carbonaceous materials,[25] or through the photo-

excitation of oxygen molecules.[54] In this study, we proposed that superoxides ($\bullet O_2^-$) might function as precursors for the generation of singlet oxygen.[26] BQ ($k_2 = 2.9 \times 10^9\ M^{-1}s^{-1}$) and bicarbonate ($k_2 = 5 \times 10^8\ M^{-1}\ s^{-1}$) as scavenger of $\bullet O_2^-$ were applied (Figure S32).[26] As shown, the degradation of 4-CP was decreased from 100% to 78% or to 12% after adding 1 and 2 mM BQ, respectively. Besides BQ, sodium bicarbonate as the scavenger of $\bullet O_2^-$ also influenced the degradation 4-CP.

Since, both BQ (OH•, $k_2 = 1.2 \times 10^9\ M^{-1}s^{-1}$) and bicarbonate (•OH, $k_2 = 3 \times 10^8\ M^{-1}\ s^{-1}$) can also react other free radicals, therefore the presence of $\bullet O_2^-$ was further confirmed from the EPR analysis. As shown in Figure 3B, the characteristic signals of DMPO-O_2 adduct appeared only in ethanol due to the extra stability of $\bullet O_2^-$ in organic solvent. The absence of DMPO-O_2 adduct in water (Figure S22), might be related to the transformation of $\bullet O_2^-$ to singlet oxygen. Additionally, the generated superoxide is expected to produce H_2O_2, during the generation of singlet oxygen.[55] Molybdate salt rapidly reacts with H_2O_2 to produce peroxymolybdate complex, which can be easily detected in the UV specra.[56] As shown in Figure S33, the adsorption for peroxymolybdate complex gradually increased in the first 10 minutes and then was hardly detected after extending the reaction time. These results thus confirmed the intermediate role of $O_2^{\bullet-}$ during the generation of singlet oxygen.

XPS analysis were performed for the CuO, CuO/Fe_3O_4 and CuOMgO/Fe_3O_4 catalysts to investigate the changes in the oxidation state of Cu after the incorporation of MgO (Figure S34). From the deconvoluted peaks of Cu $2p_{3/2}$, the peaks for CuO and CuO/Fe_3O_4 at the binding energy (B.E) of 932.03−934.04 eV were assigned to +2 oxidation state of copper (Figure S34 A,B).[9–10,57] In contrast, the Cu $2p_{3/2}$ spectra for CuOMgO/Fe_3O_4 catalyst shifted toward higher B.E side i.e. 0.84 eV from CuO and 1.06 eV from CuO/Fe_3O_4 (Figure S34 C). This shifting clearly demonstrated that the Cu^{2+} cation in CuOMgO/Fe_3O_4 catalyst is more electron deficient

and thus suggested the oxidation of Cu^{2+} to Cu^{3+} species.[58] After reaction, the proportion of proposed Cu^{3+} ions decreased from 48% to 37% and that of Cu^{2+} ions increased from 52% to 63% (Figure S34 C,D).This change is probably attributed to the electron transfer from PMS to $Cu^{(III)}$, during the generation of singlet oxygen.

Therefore, together with all characterizations on the Cu species in $CuOMgO/Fe_3O_4$, a reaction pathway based on $O_2^{\bullet-}$ was proposed for the generation of $^1O_2$ (Eqs. 5−9). At first, the incorporation of MgO with extensive hydroxyl groups facilitating the generation of Cu–OH complex, a critical step for PMS activation. The high valent electron deficient copper $[\equiv Cu^{(III)}–OH]^{II}$ reacts with PMS at the surface of $CuOMgO/Fe_3O_4$ and generates a metastable copper intermediate $[\equiv Cu^{(III)}– O–O–SO_3]^{I}$ through outer-sphere complexation (Eq.5). Afterwards, the electron deficient center of copper produce $O_2^{\bullet-}$ after accepting electron from another PMS (HSO_5^-) molecule and thus breaks the coordination bond of metastable $[\equiv Cu^{(III)}– O–O–SO_3]^{I}$ intermediate (Eq. 6). Later, $^1O_2$ is generated from the direct oxidation of $O_2^{\bullet-}$ by the $\equiv Cu^{(III)}$, which is thermodynamically feasible (E_o $Cu^{(III)}/Cu^{(II)}$ 2.3 V vs. E_o $O_2^{\bullet-}/^1O_2$ −0.34 V) or from recombination of two superoxide anions radicals (Eqs. 7−8). This activation mechanism is similar to Mn–Fe oxides induced PMS/PDS activation,[26,32] and the ultimate electron transfer from PMS molecule to electron deficient $\equiv Cu^{(III)}$ center endorsed the generation of superoxide and then singlet oxygen.

$$[\equiv Cu^{(III)}–O\cdots H]^{II} + HO\cdots O–SO_3^- \rightarrow [\equiv Cu^{(III)}– O–O–SO_3]^{I} + H_2O \quad k_1 \qquad (5)$$

$$2[\equiv Cu^{(III)}–O–O–SO_3]^{I} + 3H_2O + HO–O–SO_3^- \rightarrow 2[\equiv Cu^{(II)}–OH]^{I} + 2O_2^{\bullet-} + 7H^+ + 3SO_4^{2-} \quad k_2 \qquad (6)$$

$$[\equiv Cu^{(III)}–O–O–SO_3]^{I} + O_2^{\bullet-} + OH^- \rightarrow [\equiv Cu^{(II)}–OH]^{I} + SO_4^{2-} + 3^1O_2 \qquad k_3 \qquad (7)$$

$$2O_2^{\bullet-} + 2H_2O \rightarrow 2^1O_2 + H_2O_2 + 2OH^- \qquad k_4 \qquad (8)$$

$$4\text{-CP} + {}^1O_2 \rightarrow CO_2 + H_2O + \text{products} \qquad k_5 \qquad (9)$$

Kinetic Study

The kinetics for the above mechanism were established after changing the concentration of PMS and catalyst dosage (Figure S35 and Figure S36). The study demonstrated that the degradation of 4-CP increased at higher concentrations of PMS or catalyst dosages. The degradation rate constant (k_{obs}) at a given PMS concentration and CuOMgO/Fe_3O_4 amount was calculated after applying pseudo first-order kinetic rate equation. Then the curve fitting between ln[$k_{,obs}$] vs. ln[PMS]$_o$ or ln[CuOMgO/Fe_3O_4]$_o$ was established (inset, Figure S36). A good linear correlation for ln[k_{obs}] vs. ln[PMS]$_o$ (R^2 0.98) and ln[$k_{,obs}$] vs. [CuOMgO/Fe_3O_4]$_o$ (R^2 0.94) was established with slopes of 1.107 and 0.89 respectively, suggesting that the kinetic orders (n) of both process were close to 1. The first order of [PMS]$_o$ and [CuOMgO/Fe_3O_4]$_o$ could be assumed for reactions (Eqs. 5 and 6). Since Eq. 5 depend only on the [CuOMgO/Fe_3O_4]$_o$ at an initial excess amount of [PMS]$_o$, and thus can be considered pseudo first order reaction. On the other hand, the [CuOMgO/Fe_3O_4] in Eq. 6 was irrelevant and the reaction completely depend on the [PMS]. The kinetic studies recommended that the catalytic process totally depend upon the generation of metastable copper intermediate (Eq.5), primarily related to the adsorption and heterogeneous surface activation of PMS. Therefore, we applied Langmuir-Hinshelwood (L-H) model,[26] to confirm the role of surface mediated reactions/adsorption in CuOMgO/Fe_3O_4+PMS system (Figure S37-38). The well fitted L-H model with excellent R^2 (0.97) after plotting 1/k_{obs} against [PMS]$_o$ (Figure S38 A), suggested that the adsorption of PMS on the surface of CuOMgO/Fe_3O_4 to generate metastable [$\equiv Cu^{(III)}-O-O-SO_3]^1$ intermediates play important role in the in the enhanced catalytic activity and generation of $^1O_2$.

Advantages of Non-Radical Process

The incorporation of redox-inactive MgO not only influences the reaction mechanism but also changes some of the properties of heterogeneous catalyst such as stability. As disclosed above, the leaching of both Cu^{2+} and Fe^{2+} ions was better controlled in CuOMgO/Fe_3O_4 as compared to CuO or CuO/Fe_3O_4 (Table S2). This small leaching of metals ions also influenced the stability of CuOMgO/Fe_3O_4. As shown in Figure 3C, the reused CuO/Fe_3O_4 catalyst induced a continuous decrease in the removal of 4-CP after each circle, whereas CuOMgO/Fe_3O_4 remained stable with approximately 100% removal in all reuse experiments. Furthermore, the stability of the catalysts were also evaluated after comparing the structure changes before and after the reaction. As shown in Figure S39 A, certain XRD peaks of CuO/Fe_3O_4 structure completely disappeared after the 5th cycle, suggesting a poor structure stability during the catalytic reaction. In contrast, the XRD spectra of CuOMgO/Fe_3O_4 remained the same even after the 5th cycle, with only a small decrease in the intensity for certain side peaks (Figure S39 B). These results were also consistent with a much lower leaching of copper ions when MgO was incorporated (Figure S40). Therefore, the incorporation of MgO not only enhanced the reactivity of Cu in the CuOMgO/Fe_3O_4, but also induced better stability with a smaller leaching amount and good reusability.

The performance of AOPs including PMS/PS system is strongly correlated with solution pH.[10] As shown (Figure S41), the performance of CuOMgO/Fe_3O_4+PMS system remained stable (100% removal) in the initial pH 5.0-10, and then decreased to 80% when the initial pH was raised to12.0. These results are quite different from the activity of Rose Bengal (RB), a well-known $^1O_2$-mediation system,[35] when being applied under the same conditions (Figure S42). Obviously these two system had so many differences, and three dominant factors can be considered: 1) the buffer capacity of CuOMgO/Fe_3O_4, 2) the leaching of active component and 3) the interaction of catalyst, PMS and target compound.

Firstly, the removal trend of 4-CP under different initial pHs corresponded to the final pH of solution (Figure S43). As shown, the eventual pH after the reaction remained stable at pH 9. 0 ± 0.5 in the initial pHs ranged from 5.0 to10.0. Thus the relatively constant performance (k= 0.12 ~ 0.16 min^{-1}) in this pH range may be partly attributed to the buffer ability of CuOMgO/Fe_3O_4. In the case of RB, this phenomena does not exist. Secondly, the lower activity at pH 3.0 could be attributed to the leaching of heterogeneous catalysts (Figure S44 A), whereas 22 ppm Cu and 8 ppm Fe leaching was observed for CuOMgO/Fe_3O_4. On the other hand, the low catalytic activity at pH 12.0 could be explained by the fact that the surface of the CuOMgO/Fe_3O_4 becomes more negatively charged and consequently results in electrostatic repulsion between the negatively charged CuOMgO/Fe_3O_4 (pH_{ZPC}=9.30, Figure S45), deprotonated 4-CP (pk_a=9.18) and SO_5^{2-} (pk_a=9.41). Furthermore, the active sites on the surface of CuOMgO/Fe_3O_4 might also be passivated due the deposition of hydroxides layers (Figure S46). In contrast, singlet oxygenated system (RB system) indicate significant improvements in the degradation of 4-CP at high pH, because the above negative effects did not emerge (Figure S42). This conclusion was further supported by the nonlinear relationship between the degradation rate constants k and F factor calculated from Eq. 10,[26] (Figure S47), which also suggested the that the decrease of 4-CP degradation at high pH was resulted from the surface electrostatic repulsion.

$$F= k_w/[H^+] + k_a \qquad (10)$$

Bromate (BrO_3^-) is one of the most alarming byproduct of AOPs, listed as possible human carcinogen, and it is commonly generated in free radical AOPs.[36] Considering the threat level of bromate, CuOMgO/Fe_3O_4+PMS system was evaluated for the generation of BrO_3^- after reacting in brominated water (Figure S48). As shown, the generation of huge amount of BrO_3^- in Co^{2+}/PMS system was accounted for the reaction of $SO_4^{\bullet-}$ radicals and bromide ions. In

contrast, no BrO_3^- was detected in CuOMgO/Fe_3O_4+PMS system which highlighted the advantage of non-free radical process over free radical process.

Inorganic anions such as Cl^- and CO_3^{2-} are common background electrolytes in real wastewater. Normally, their existence negatively influences the efficiency of radical-based advanced oxidation processes. Both •OH and SO_4^{-}• radicals tend to be rapidly scavenged by halogens ions with a high reaction rate constants ($k_{SO4-\bullet/Cl-}$= (3.2 ± 0.2) × 10^8 $M^{-1}s^{-1}$, $k_{\bullet OH/Cl-}$ = 4.2 × 10^9 $M^{-1}s^{-1}$).[24,59–60] Therefore, the influence of inorganic anions on the efficiency loss of the CuOMgO/Fe_3O_4+PMS system was also investigated. Figure 3D depicts that the Cl^-, NO_3^-, SO_4^{2-} and CH_3COO^- anions demonstrated negligible influences on the degradation efficiency of 4-CP. Due to the fact that •OH and SO_4^{-}• radicals were not produced, the small scavenging of CO_3^{2-} and HCO_3^- (~10-15%) might be from the selective scavenging of $\bullet O_2^-$ anions (CO_3^{2-}, k_2= 5 × 10^8 $M^{-1}s^{-1}$).[26] Additionally, humic acid (HA, a typical NOM), which is excessively found in wastewater and is considered to be another free radical scavenger.[7] The analysis showed that HA decreased the degradation of 4-CP in the initial 20 minutes. However, the scavenging effects became less important when the reaction time was extended to 40 minutes (Figure S49). The decrease in the initial 20 minutes might be related to the adsorption of HA on the surface of catalyst which could minimize the complexation of PMS to generate $^1O_2$. On extending the reaction time, enough $^1O_2$ would be produced to proceed the reaction smoothly.

Structure Activity Relationship and Degradation Pathway

The degradation rate constants (k_{obs}) for 14 substituted phenols were calculated in CuOMgO/Fe_3O_4+PMS system after applying pseudo-first order kinetics. The calculated k_{obs} in CuOMgO/Fe_3O_4+PMS system were then compared with literature values obtained for similar reactions in aqueous solution (Table S6).[60-62]Among the studied substituted phenols, 4-MeCONH exhibited the maximum degradation rate with k_{obs} (0.168 min^{-1}), while 4-NO_2

phenol demonstrated the slowest oxidation with k_{obs} (0.037 min^{-1}). To describe the quantitative effect of substitution on the degradation rate of these phenols, the obtained k_{obs} values were changed to relative rates (k_{rel}) using 4-CP as the reference compound, as described in Eq 11.

$$\log k_{rel} = \log \frac{kobs}{k4-CP} \qquad (11)$$

Whereas k_{obs} is the pseudo-first-order degradation rate of different substituted phenols and $k_{4\text{-}CP}$ is the observed rate constant of 4-CP. This type of normalization is very effective to give satisfactory structure-activity relationship in persulfate activation. Using this approach, we calculated $\log k_{rel}$ along with other substituent descriptor variables (i.e., Hammett constants σ, σ+ and σ− and $E_{1/2}$) (Table S7). The obtained results were then compared to the substituent descriptor variables of Wang et al,[60] using the degradation of similar substituted phenols in PMS activated system (Table S7). In the oxidative reactions of substituted phenols, Hammett constants (i.e. σ, σ^+ and σ^-) were mostly used to quantitatively correlate the electron donating (large negative value) or electron withdrawing (large positive value) properties of substituents.[61-63] Of the three Hammett constants (i.e. σ, σ^+ and σ^-), σ^+ give relatively good correlation (Figure 4 A and Figure S50 A,B) with linear regression as expressed in Eq. 12. The decrease in the oxidation rates of phenolic compounds with the increase of σ^+ (Table S7) suggested a typical electrophilic reaction between the reactive species ($^1O_2$) and substituted phenols.

$$\text{Log}k_{rel} = 0.344\ (\pm\ 0.103)\ -0.752\ (\pm\ 0.243)\times\sigma^+\ R^2 = 0.72 \qquad (12)$$

On the other side, half-wave potential ($E_{1/2}$) reflects the ability of electron transfer as limiting step during the oxidation reactions and the values obtained are often used to construct quantitative structure-activity relationships (QSARs). Previously, the good linear relationship between the degradation rate of substituted phenol ($\log k_{rel}$) and $E_{1/2}$ was used to predict the rate limiting steps in CNT/PS system.[62] In the case of CuOMgO/Fe_3O_4+PMS, a linear relationship

was established among the values of $E_{1/2}$ and logk_{rel} (Figure 4 B and Table S7). As shown, the good linear relationship between logk_{rel} and $E_{1/2}$ highlighted one electron oxidation without proton transfer as the rate limiting step during the oxidation of substituted phenols.

Meanwhile, in some cases logk_{rel} was not only correlated with the Hammett constant σ^+, but also showed good linear relationship with the pK_a values of organic contaminants,[64] which indicated that not only the electron transfer but the proton transfer also contribute to oxidation, as in the case of C-H bond cleavage by the non-selective radicals. In the system of CuOMgO/Fe_3O_4+PMS however, there was no clear correlation between the logk_{rel} and pK_a (Figure 4 C). This phenomenon together with the linear correlation of logk_{rel} σ^+ and $E_{1/2}$ thus suggested the electron transfer mediated by $^1O_2$ was the dominant oxidation process for organic contaminants.

Additionally, kinetic isotopic effect (KIE) was also applied to reveal the electron transfer process between the organic substrate and singlet oxygen. In general, 2 <KIE< 7 can be used to predict the C-H bond cleavage, which is typical for •OH radicals in hydrogen atom transfer (HAT) process when attacking the aromatic ring. In contrast, the small KIE (0.7<KIE<1.5) indicates that the hydrogen atom transfer is not the limiting step. In the system of CuOMgO/Fe_3O_4+PMS, we compared the reaction rate constant with two substrate of phenol and phenol-d5 (Figure 4 D), and calculated KIE=1 (inset of Figure 4 D). This result once again suggested that the oxidation of aromatic rings was dominantly through one electron transfer process by $^1O_2$, rather than HAT process as •OH mediated oxidations. This electron transfer was highly consistent with our observation of the linear relationship of logk_{rel} and σ^+ but no correlation on pK_a in QSARs study.

To sum up, the theoretical calculation based on the correlation of logk_{rel} with σ^+ and $E_{1/2}$ showed that the degradation of 4-CP began with the electron transfer from target compound to

595 $^1O_2$. Additionally, the high one electron standard reduction potential of $^1O_2/^{\bullet-}O_2$ (E_1^o 0.79 V
596 NHE) than phenoxy/phenolate couple (E_1^o 0.60 V NHE) also made this process
597 thermodynamically more feasible.[62] Thus the electron transfer likely generated a transition
598 complex with a small amount of charge-transfer character (Figure S51, step 2), during which
599 the endoperoxide charged complex as result of cyclic-addition might act as highly unstable
600 intermediate. The good linear relationship and the kinetic isotopic effect (KIE) further
601 supported that this electron transfer mediated oxidation process by $^1O_2$ is the key step. Based
602 on GC-MS study, the identified products included chlorophenols, 1,4-benzoquinone and some
603 small open chain products (Table S8), while the additional products like di- or tri-
604 chlorophenols were not observed (Figure S51, step 1), which was further supported by the good
605 TOC removal efficiency (Table S2).

606 **Environmental Implications**

607 For the first time, we found that the incorporation of MgO not only enhanced the catalytic
608 properties but also modified the persulfate oxidation process from classical free radical
609 mechanism to non-radical mechanism. Normally in real water applications, heterogeneous
610 catalysts are loaded onto stable inorganic supports, which are commonly redox-inactive metal
611 oxides. Therefore, addressing the functional roles of these redox-inactive metal oxides in
612 regulating the environmental catalysts is of great importance. Secondly, we comprehensively
613 investigated the unique behaviour of this non-radical process from the view of kinetics,
614 interferences from water matrix, stability at broad pHs and the generation of toxic by-products
615 in complex water matrix. Interestingly, no toxic BrO_3^- was produced even in the presence of
616 spiked Br^-, suggesting another advantage of $^1O_2$ dominated process over classical radical ones.
617 The linear free energy relationships (LFERs) between the degradation rate constant of 14
618 substituted phenols and conventional descriptor variables (i.e. Hammett constant σ, σ^-, σ^+) in
619 quantitative structure activity relationship (QSARs) study not only offered insights into the

620 reaction mechanism that one electron oxidation is the dominant process by $^1O_2$, in which proton
621 transfer is not accompanied, but also offered clues to predict the reactivity of most common
622 phenol-substituted contaminants in non-radical PMS oxidation.

623 **ASSOCIATED CONTENT**

624 The supporting information i.e. Table S1-S8, Text S1-S7 and Figure S1-S52 were also given
625 in the supporting information. This information is available free of charge at
626 http://www.pubs.acs.org.

627 **AUTHOR INFORMATION**

628 **Corresponding Author**

629 *Phone: +8613476079416, E-mail address: zqchen@hust.edu.cn

630 **Notes:** The authors declare no competing financial interests.

631

632 ACKNOWLEDGMENT

633 This work was financially supported by the National Key R&D Program of China (No.
634 2018YFC1802302), the National Science Foundation of China (No. 21671072), the
635 Fundamental Research Funds for the Central Universities (No. 2019kfyRCPY058), and
636 Chutian Scholar Foundation from Hubei province. The authors also acknowledge the
637 Analytical and Testing Centre of Huazhong University of Science and Technology for SEM,
638 FTIR, XRD, XPS and elemental analyses.

639

640 **References**

641 1. Liu, X. W.; Zhang, T. Q.; Zhou, Y. C.; Fang, L.; Shao, Y. Degradation of atenolol by
642 UV/peroxymonosulfate: kinetics, effect of operational, parameters and mechanism.
643 Chemosphere **2013**, *93* (11), 2717−2724.

644 2. Yang, S. Y.; Wang, P.; Yang, X.; Shan, L.; Zhang, W. Y.; Shao, X. T.; Niu, R.
645 Degradation efficiencies of azo dye Acid Orange 7 by the interaction of heat, UV and
646 anions with common oxidants: Persulfate, peroxymonosulfate and hydrogen peroxide.
647 J. Hazard. Mater. **2010**, *179* (1−3), 552−558.
648 3. Chen, W. S.; Huang, C. P. Mineralization of aniline in aqueous solution by
649 electrochemical activation of persulfate. Chemosphere **2015**, *125*, 175−181.
650 4. Anipsitakis, G. P.; Dionysiou, D. D. Degradation of organic contaminants in water with
651 sulfate radicals generated by the conjunction of peroxymonosulfate with cobalt.
652 Environ. Sci. Technol. **2003**, *37* (20), 4790−4797.
653 5. Yang, Q. J.; Choi, H.; Dionysiou, D. D. Nanocrystalline cobalt oxide immobilized on
654 titanium dioxide nanoparticles for the heterogeneous activation of peroxymonosulfate.
655 Appl. Catal., B **2007**, *2*, 170−178.
656 6. Liu, H. Z.; Bruton, T. A.; Doyle, F. M.; Sedlak, D. L. In situ chemical oxidation of
657 contaminated groundwater by persulfate: Decomposition by $Fe^{(III)}$ and $Mn^{(IV)}$
658 containing oxides and aquifer materials. Environ. Sci. Technol. **2014**, *48* (17),
659 10330−10336.
660 7. Zhang, T.; Zhu, H.; Croué, J. P. Production of sulfate radical from peroxymonosulfate
661 induced by a magnetically separable $CuFe_2O_4$ spinel in water: efficiency, stability, and
662 mechanism, Environ. Sci. Technol. **2013**, *47* (6) 2784-2791.
663 8. Li, Y.; Guo, L.; Huang, D.; Jawad, A.; Chen, Z.; Yang, J.; Liu, W.; Shen, Y.; Wang,
664 M.; Yin, G. Support-dependent active species formation for CuO catalysts: Leading to
665 efficient pollutant degradation in alkaline conditions. J. Hazard. Mater. **2017,** *328*, 56-
666 62.

9. Feng, Y.; Deli W.; Yu D.; Tong Z.; Kaimin S. Sulfate radical-mediated degradation of sulfadiazine by $CuFeO_2$ rhombohedral crystal-catalyzed peroxymonosulfate: synergistic effects and mechanisms. Environ. Sci. Technol. **2016**, *50*, 3119-3127.
10. Lei, Y.; Chen, C.S.; Tu, Y.J.; Ding, Y. Heterogeneous degradation of organic pollutants by persulfate activated by CuO-Fe_3O_4: mechanism, stability and effects of pH and bicarbonate ions, Environ. Sci. Technol. **2015**, *49*, 6838-6845.
11. Huang, G. X.; Wang, C. Y.; Yang, C. W.; Guo, P. C.; Yu, H. Q. Degradation of bisphenol A by peroxymonosulfate catalytically activated with $Mn_{1.8}Fe_{1.2}O_4$ nanospheres: synergism between Mn and Fe. Environ. Sci. Technol. **2017,** *51* (21), 12611-12618.
12. Fang, G.D.; Liu, C.; Gao, J.; Dionysiou, D.D.; Zhou, D.M. Manipulation of persistent free radicals in biochar to activate persulfate for contaminant degradation. Environ. Sci. Technol. **2015**, *49* (9), 5645-5653.
13. Sun, H.Q.; Kwan, C.; Suvorova, A.; Ang, H.M.; Tade, M.O.; Wang, S.B. Catalytic oxidation of organic pollutants on pristine and surface nitrogen-modified carbon nanotubes with sulfate radicals. Appl. Catal. B Environ. **2014**, *154*, 134-141.
14. Chen, H.; Carroll, K.C. Metal-free catalysis of persulfate activation and organic-pollutant degradation by nitrogen-doped graphene and aminated graphene. Environ. Pollut. **2016**, *215*, 96-102.
15. Duan, X.G.; Su, C.; Zhou, L.; Sun, H.Q.; Suvorova, A.; Odedairo, T.; Zhu, Z.H.; Shao, Z.P.; Wang, S.B. Surface controlled generation of reactive radicals from persulfate by carbocatalysis on nanodiamonds. Appl. Catal. B Environ. **2016**, *194*, 7-15.
16. Lin, S. S.; Gurol, M. D. Catalytic decomposition of hydrogen peroxide on iron oxide: Kinetics, mechanism, and implications. Environ. Sci. Technol. **1998**, *32* (10), 1417−1423.

17. Kwan, W. P.; Voelker, B. M. Decomposition of hydrogen peroxide and organic compounds in the presence of dissolved iron and ferrihydrite. Environ. Sci. Technol. **2002**, *36* (7), 1467−1476.
18. Furman, O. S.; Teel, A. L.; Watts, R. J. Mechanism of base activation of persulfate. Environ. Sci. Technol. **2010**, *44* (16), 6423−6428.
19. Ji, Y.; Dong, C.; Kong, D.; Lu, J. New insights into atrazine degradation by cobalt catalyzed peroxymonosulfate oxidation: kinetics, reaction products and transformation mechanisms, J. Hazard. Mater. **2015**, *285*, 491-500.
20. Ross, A.B.; Neta, P. Rate constants for reactions of inorganic radicals in aqueous solution. US department of commerce, national bureau of standards Washington D. C. **1979**.
21. Zhang, T.; Chen, Y.; Wang, Y.; Le Roux, J.; Yang, Y.; Croué, J. P. Efficient peroxydisulfate activation process not relying on sulphate radical generation for water pollutant degradation. Environ. Sci. Technol. **2014,** *48* (10), 5868-5875.
22. Ahn, Y. Y.; Yun, E. T.; Seo, J. W.; Lee, C.; Kim, S. H.; Kim, J. H.; Lee, J. Activation of peroxymonosulfate by surface-loaded noble metal nanoparticles for oxidative degradation of organic compounds. Environ. Sci. Technol. **2016,** *50* (18), 10187-10197.
23. Duan, X.; Sun, H.; Shao, Z.; Wang, S. Nonradical reactions in environmental remediation processes: Uncertainty and challenges. App. Catal. B: Environ. **2018,** *224*, 973-982.
24. Feng, Y.; Lee, P. H.; Wu, D.; Shih, K. Surface-bound sulfate radical-dominated degradation of 1,4-dioxane by alumina-supported palladium (Pd/Al_2O_3) catalyzed peroxymonosulfate. Water Res. **2017,** *120*, 12-21.

25. Cheng, X.; Hongguang G.; Yongli Z.; Xiao W.; Yang L. Non-photochemical production of singlet oxygen via activation of persulfate by carbon nanotubes." Water Res. **2017**, *113*, 80-88.

26. Zhu, S.; Li, X.; Kang, J.; Duan, X.; Wang, S. Persulfate activation on crystallographic manganese oxides: Mechanism of singlet oxygen evolution for nonradical selective degradation of aqueous contaminants. Environ. Sci. Technol. **2019,** *53*, (1), 307-315.

27. Tian, W.; Zhang, H.; Qian, Z.; Ouyang, T.; Sun, H.; Qin, J.; Tadé, M. O.; Wang, S. Bread-making synthesis of hierarchically Co@C nanoarchitecture in heteroatom doped porous carbons for oxidative degradation of emerging contaminants. App. Catal. B: Environ: **2018,** *225*, 76-83.

28. Tian, X.; Gao, P.; Nie, Y.; Yang, C.; Zhou, Z.; Li, Y.; Wang, Y. A novel singlet oxygen involved peroxymonosulfate activation mechanism for degradation of ofloxacin and phenol in water. Chem. Comm. **2017,** *53*, (49), 6589-6592.

29. Yang, Z.; Dai, D.; Yao, Y.; Chen, L.; Liu, Q.; Luo, L. Extremely enhanced generation of reactive oxygen species for oxidation of pollutants from peroxymonosulfate induced by a supported copper oxide catalyst. Chem. Eng. J. **2017,** *322*, 546-555.

30. Jiang, M.; Lu, J.; Ji, Y.; Kong, D. Bicarbonate-activated persulfate oxidation of acetaminophen. Water Res. **2017,** *116*, 324-331.

31. Khan, A.; Wang, H.; Liu, Y.; Jawad A.; Ifthikhar, J.; Liao, Z.; Wang, T.; Chen. Z. Highly efficient α-Mn_2O_3@α-MnO_2-500 nanocomposite for peroxymonosulfate activation: comprehensive investigation of manganese oxides J. Mater. Chem. A, **2018**, *6*, 1590–1600.

32. Yu, L.; Zhang, G.; Liu, C.; Lan, H.; Liu, H.; Qu, J. Interface stabilization of undercoordinated iron centers on manganese oxides for nature-inspired peroxide activation. ACS Catal. **2018**, *8* (2), 1090-1096.

739 33. Peng, W.; Liu, J.; Li, C.; Zong, F.; Xu, W.; Zhang, X.; Fang, Z.; A multipath
740 peroxymonosulfate activation process over supported by magnetic CuO-Fe_3O_4
741 nanoparticles for efficient degradation of 4-chlorophenol. Korean J. Chem. Eng. **2018**,
742 *35*, 1662–1672.
743 34. Saputra, E.; Muhammad, S.; Sun, H.; Ang, H. M.; Tadé, M. O.; Wang, S., Different
744 crystallographic one-dimensional MnO_2 nanomaterials and their superior performance
745 in catalytic phenol degradation. Environ. Sci. Technol. **2013,** *47*, (11), 5882-5887.
746 35. Brame, J.; Long, M.; Li, Q.; Alvarez, P. Trading oxidation power for efficiency:
747 differential inhibition of photo-generated hydroxyl radicals versus singlet oxygen.
748 Water Res. **2014**, *60*, 259−266.
749 36. Zhang, T.; Chen, W.; Ma, J.; Qiang, Z. Minimizing bromate formation with cerium
750 dioxide during ozonation of bromide-containing water. Water Res. **2008,** *42*, (14),
751 3651-3658.
752 37. Liang, C.; Huang, C. F.; Mohanty, N.; Kurakalva, R. M. A rapid spectrophotometric
753 determination of persulfate anion in ISCO. Chemosphere **2008,** *73* (9), 1540-1543.
754 38. Yuan, Z.; Lina W.; Junhua W.; Shuixin X.; Ping C.; Zhaoyin H.; Xiaoming Z.
755 Hydrogenolysis of glycerol over homogenously dispersed copper on solid base
756 catalysts. App. Catal. B: Environ. **2011**,*101*, 3, 431-440.
757 39. Van Der Grift, C. J. G.; Wielers, A. F. H.; Jogh, B. P. J.; Van Beunum, J.; De Boer, M.;
758 Versluijs-Helder, M.; Geus, J. W. Effect of the reduction treatment on the structure and
759 reactivity of silica-supported copper particles. J. Catal. **1991,** *131* (1), 178-189.
760 40. Zabilskiy, M.; Djinović, P.; Erjavec, B.; Dražić, G.; Pintar, A. Small CuO clusters on
761 CeO_2 nanospheres as active species for catalytic N_2O decomposition. App. Catal. B:
762 Environ. **2015,** *163*, 113-12.

763 41. Zhao, S.; Li, K.; Jiang, S.; Li, J. Pd–Co based spinel oxides derived from pd
764 nanoparticles immobilized on layered double hydroxides for toluene combustion. App.
765 Catal. B: Environ. **2016,** *181*, 236-248.
766 42. Deng, Y.; Handoko, A. D.; Du, Y.; Xi, S.; Yeo, B. S. In situ Raman spectroscopy of
767 copper and copper oxide surfaces during electrochemical oxygen evolution reaction:
768 identification of Cu^{III} oxides as catalytically active species. ACS Catal. **2016,** *6*, (4),
769 2473-2481.
770 43. Yun, E.T.; Lee, J. H.; Kim, J.; Park, H.D.; Lee, J. Identifying the nonradical mechanism
771 in the peroxymonosulfate activation process: singlet oxygenation versus mediated
772 electron transfer. Environ. Sci. Technol. **2018,** *52*, (12), 7032-7042.
773 44. Lee, H.; Kim, H. i.; Weon, S.; Choi, W.; Hwang, Y. S.; Seo, J.; Lee, C.; Kim, J. H.
774 Activation of persulfates by graphitized nanodiamonds for removal of organic
775 compounds. Environ. Sci. Technol. **2016,** *50*, (18), 10134-10142.
776 45. Duan, X.; Ao, Z.; Zhou, L.; Sun, H.; Wang, G.; Wang, S. Occurrence of radical and
777 nonradical pathways from carbocatalysts for aqueous and nonaqueous catalytic
778 oxidation. App. Catal. B: Environ. **2016,** *188*, 98-105.
779 46. Li, C.; Huang, Y.; Dong, X.; Sun, Z.; Duan, X.; Ren, B.; Zheng, S.; Dionysiou, D. D.,
780 Highly efficient activation of peroxymonosulfate by natural negatively-charged
781 kaolinite with abundant hydroxyl groups for the degradation of atrazine. App. Catal.
782 B: Environ. **2019,** *247*, 10-23.
783 47. Zhu, Z.S.; Yu, X.J.; Qu, J.; Jing, Y.Q.; Abdelkrim, Y.; Yu, Z.Z., Preforming abundant
784 surface cobalt hydroxyl groups on low crystalline flowerlike $Co_3(Si_2O_5)_2(OH)_2$ for
785 enhancing catalytic degradation performances with a critical nonradical reaction. App.
786 Catal. B: Environ. **2020,** *261*, 118238.

787 48. Guan, Y.H.; Ma, J.; Ren, Y.M.; Liu, Y.L.; Xiao, J.Y.; Lin, L.Q.; Zhang, C., Efficient
788 degradation of atrazine by magnetic porous copper ferrite catalyzed
789 peroxymonosulfate oxidation via the formation of hydroxyl and sulfate radicals.
790 Water Res. **2013,** *47*, (14), 5431-5438.
791 49. Ren, Y.; Lin, L.; Ma, J.; Yang, J.; Feng, J.; Fan, Z., Sulfate radicals induced from
792 peroxymonosulfate by magnetic ferrospinel MFe_2O_4 (M=Co, Cu, Mn, and Zn) as
793 heterogeneous catalysts in the water. App. Catal. B: Environ. **2015,** *165*, 572-578.
794 50. Knözinger, E.; Jacob, K.H.; Singh, S.; Hofmann, P., Hydroxyl groups as IR active
795 surface probes on MgO crystallites. Surf. Sci. **1993,** *290*, (3), 388-402.
796 51. Del Arco, M.; Martin, C.; Martin, I.; Rives, V.; Trujillano, R., A FTIR spectroscopic
797 study of surface acidity and basicity of mixed Mg, Al-oxides obtained by thermal
798 decomposition of hydrotalcite. Spectrochimica Acta Part A. **1993,** *49*, (11), 1575-
799 1582.
800 52. Zhang, W.; Tay, H. L.; Lim, S. S.; Wang, Y.; Zhong, Z.; Xu, R., Supported cobalt
801 oxide on MgO: highly efficient catalysts for degradation of organic dyes in dilute
802 solutions. App. Catal. B: Environ. **2010,** *95*, (1), 93-99.
803 53. Xu, Y.; Ai, J.; Zhang, H., The mechanism of degradation of bisphenol A using the
804 magnetically separable $CuFe_2O_4$/peroxymonosulfate heterogeneous oxidation process.
805 J. Hazard. Mater. **2016,** *309*, 87-96.
806 54. Lee, J.; Hong, S.; Mackeyev, Y.; Lee, C.; Chung, E.; Wilson, L. J.; Kim, J. H.; Alvarez,
807 P. J. Photosensitized oxidation of emerging organic pollutants by tetrakis C60
808 aminofullerene-derivatized silica under visible light irradiation. Environ. Sci. Technol.
809 **2011**, *45*, 10598−10604.

55. Duan, X.; Su, C.; Miao, J.; Zhong, Y.; Shao, Z.; Wang, S.; Sun, H. Insights into perovskite-catalyzed peroxymonosulfate activation: Maneuverable cobalt sites for promoted evolution of sulfate radicals. App. Catal. B: Environ. **2018**, *220*, 626-634.

56. Chai, X. S.; Hou, Q. X.; Luo, Q.; Zhu, J. Y. Rapid determination of hydrogen peroxide in the wood pulp bleaching streams by a dual-wavelength spectroscopic method. Anal. Chim. Acta **2004**, *507* (2), 281-284.

57. Zabilskiy, M.; Djinović, P.; Tchernychova, E.; Tkachenko, O. P.; Kustov, L. M.; Pintar, A. Nanoshaped CuO/CeO_2 materials: effect of the exposed ceria surfaces on catalytic activity in N_2O decomposition reaction. ACS Catal. **2015,** *5*, (9), 5357-5365.

58. Wang, L.; Sun, Y. G.; Hu, L. L.; Piao, J. Y.; Guo, J.; Manthiram, A.; Ma, J.; Cao, A. M. Copper-substituted $Na_{0.67}Ni_{0.3-x}Cu_xMn_{0.7}O_2$ cathode materials for sodium-ion batteries with suppressed P_2–O_2 phase transition. J. Mater. Chem. A **2017,** *5*, (18), 8752-8761.

59. Lindsey, M. E.; Tarr, M. A. Inhibition of hydroxyl radical reaction with aromatics by dissolved natural organic matter. Environ. Sci. Technol. **2000**, *34* (3), 444−449.

60. Wang, L.; Jiang, J.; Pang, S.Y.; Zhou, Y.; Li, J.; Sun, S.; Gao, Y.; Jiang, C. Oxidation of bisphenol A by nonradical activation of peroxymonosulfate in the presence of amorphous manganese dioxide. Chem. Eng. J. **2018,** *352*, 1004-1013.

61. Tratnyek, P. G.; Hoigne, J. Oxidation of substituted phenols in the environment: a QSAR analysis of rate constants for reaction with singlet oxygen. Environ. Sci. Technol. **1991,** *25*, (9), 1596-1604.

62. Guan, C.; Jiang, J.; Pang, S.; Luo, C.; Ma, J.; Zhou, Y.; Yang, Y. Oxidation kinetics of bromophenols by nonradical activation of peroxydisulfate in the presence of carbon nanotube and formation of brominated polymeric products. Environ. Sci. Technol. **2017,** *51*, (18), 10718-10728.

63. Tekle-Röttering, A.; von Sonntag, C.; Reisz, E.; Eyser, C. v.; Lutze, H. V.; Türk, J.; Naumov, S.; Schmidt, W.; Schmidt, T. C. Ozonation of anilines: Kinetics, stoichiometry, product identification and elucidation of pathways. Water Res. **2016,** *98*, 147-159.

64. Sun, S.; Liu, Y.; Ma, J.; Pang, S.; Huang, Z.; Gu, J.; Gao, Y.; Xue, M.; Yuan, Y.; Jiang, J. Transformation of substituted anilines by ferrate(VI): Kinetics, pathways, and effect of dissolved organic matter. Chem. Eng. J. **2018,** *332*, 245-252.

846

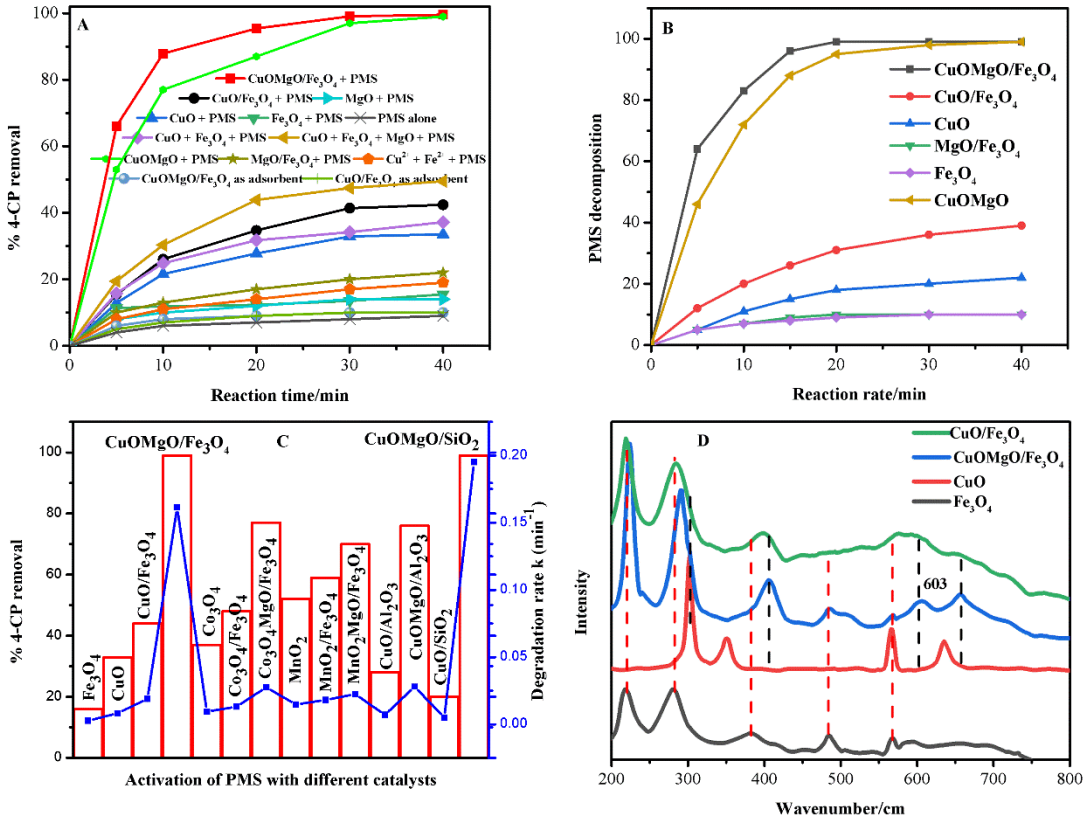

847

848 **Figure 1** (A-C) role of MgO to improve the catalytic activity and PMS utilization efficiency
849 of different metals oxides (D) Raman spectra showing the abundant lattice defects and
850 prominent peak of Cu^{3+} state in $CuOMgO/Fe_3O_4$ catalyst.

851 **Conditions:** 4-CP 40 ppm, PMS 2 mM, catalyst 0.2g/L, reaction temperature 30 ^{o}C and
852 reaction time 40 min.

853

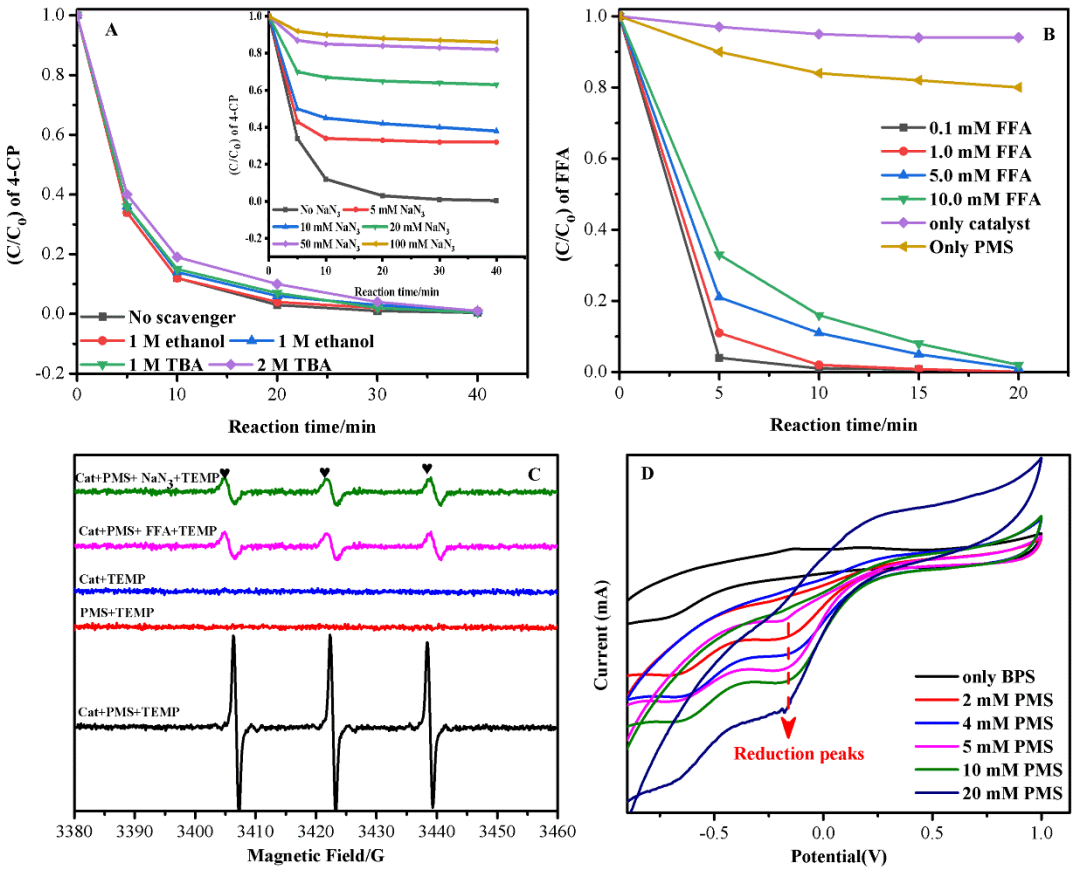

854

855 **Figure 2** (A) Influences of ethanol and TBA on the activity of CuOMgO/Fe_3O_4, (inset showing
856 the influence of NaN_3 on the activity of CuOMgO/Fe_3O_4 (B) degradation of FFA as $^1O_2$-
857 indicator (C) generation of $^1O_2$ with TEMP (D) CV plots showing the increase in the reduction
858 peak of CuOMgO/Fe_3O_4+PMS system with increasing PMS amount.

859 **Conditions:** 4-CP 40 ppm, PMS 2 mM, catalyst 0.2g/L, reaction temperature 30 ^oC and
860 reaction time 40 min.

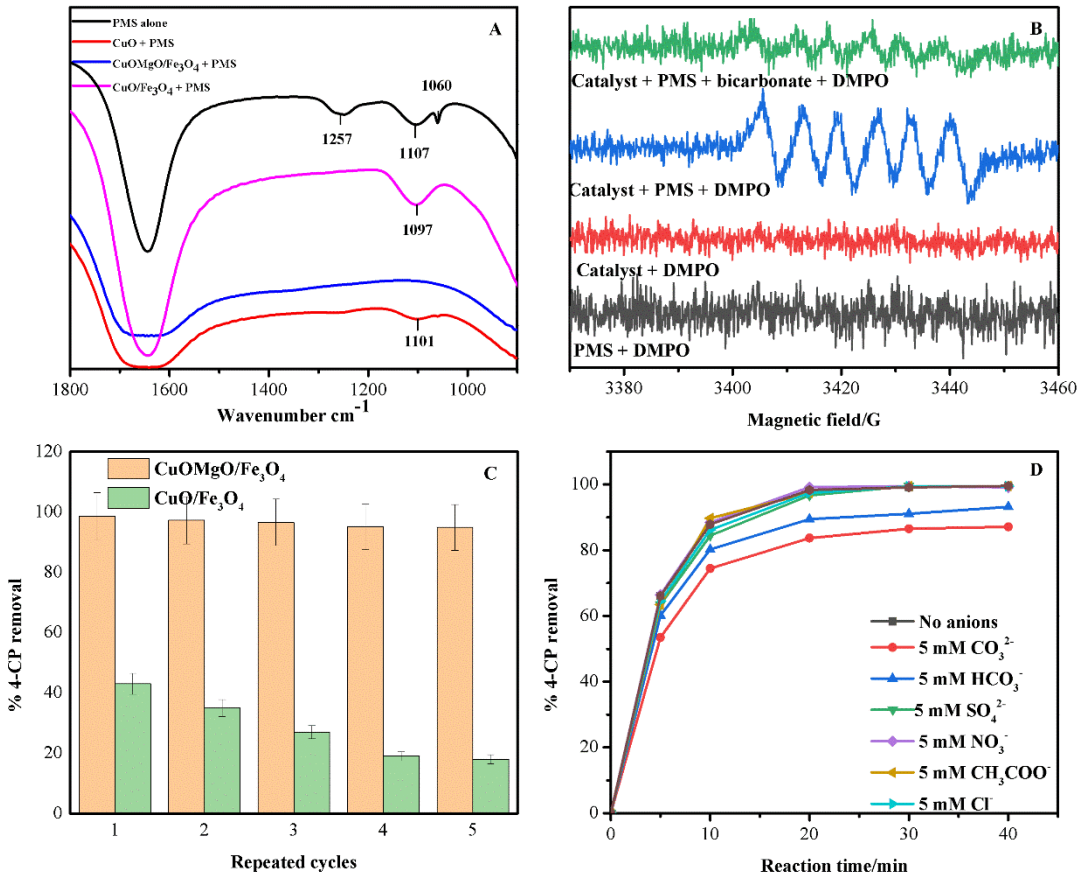

Figure 3 (A) ATR-FTIR spectra of PMS after interacting CuOMgO/Fe_3O_4, CuO/Fe_3O_4 and CuO catalysts (B) generation of DMPO-O_2 adduct in ethanol, giving strong evidence for the presence of super oxides in CuOMgO/Fe_3O_4+PMS system (C) stability of CuOMgO/Fe_3O_4, CuO/Fe_3O_4 in the recycled experiments (D) influence of anions on the catalytic activity of CuOMgO/Fe_3O_4+PMS system.

870

871

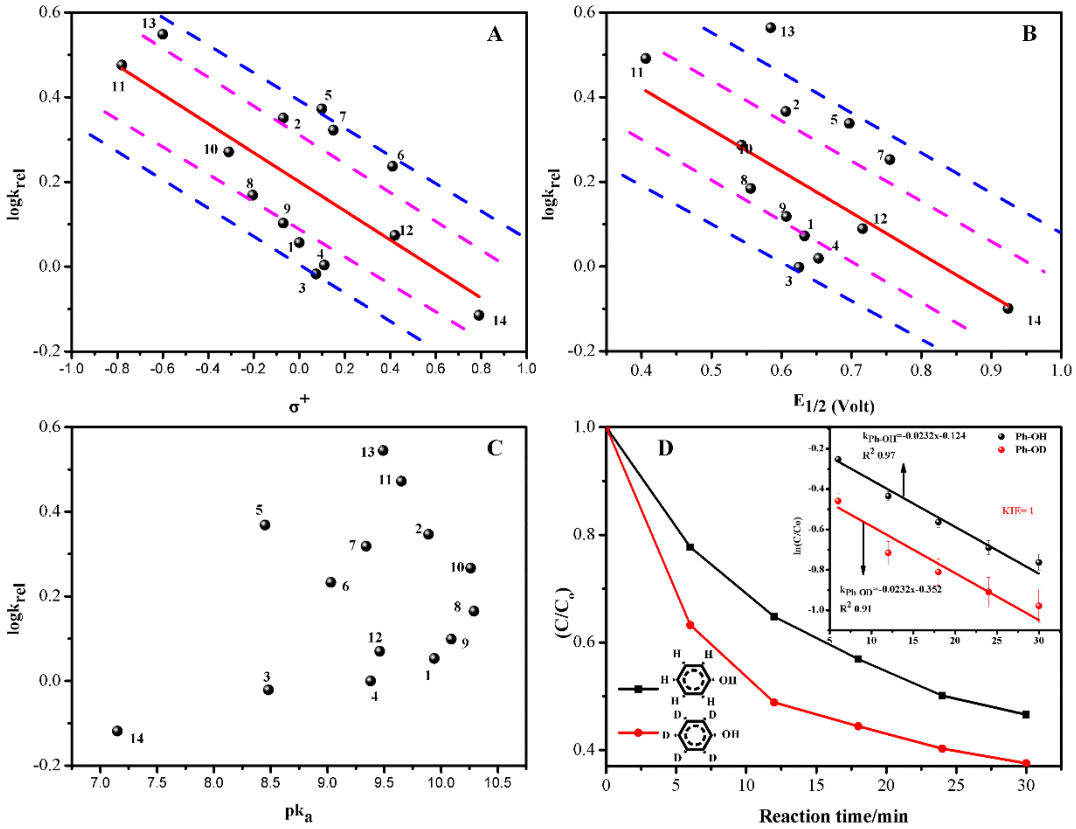

872

873 **Figure 4** Quantitative structure-activity relationships of substituted phenols for (A) Hammett
874 σ^+ constant, (B) half-wave potential ($E_{1/2}$) (C) pK_a and (D) Calculating KIE using
875 CuOMgO/Fe_3O_4+PMS system.

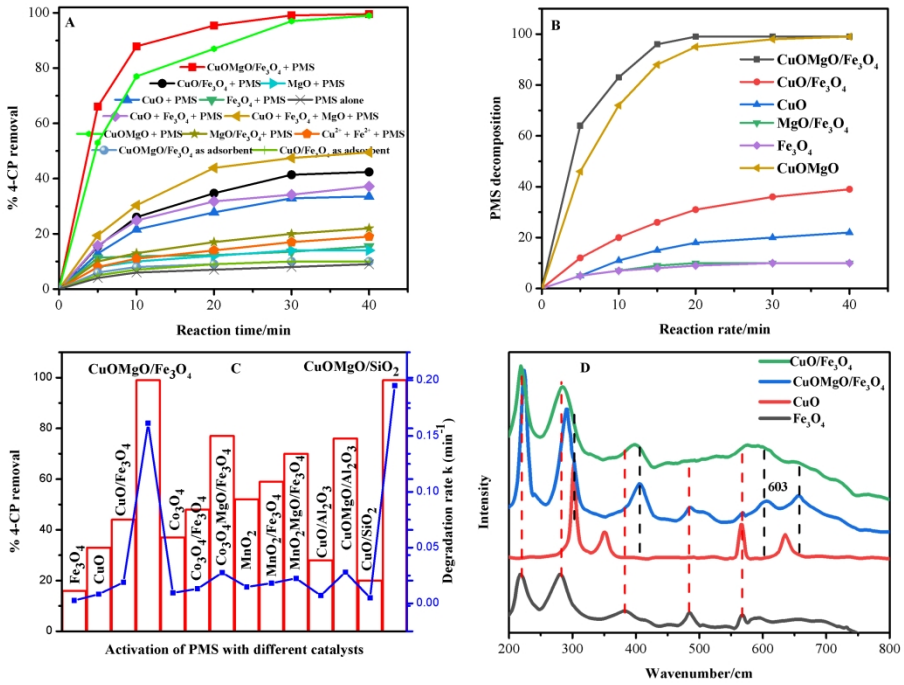

Fig.1 (A-C) role of MgO to improve the catalytic activity and PMS utilization efficiency of different metals oxides (D) Raman spectra showing the abundant lattice defects and prominent peak of Cu3+ state in CuOMgO/Fe3O4 catalyst.Conditions: 4-CP 40 ppm, PMS 2 mM, catalyst 0.2g/L, reaction temperature 30 oC and reaction time 40 min.

216x159mm (400 x 400 DPI)

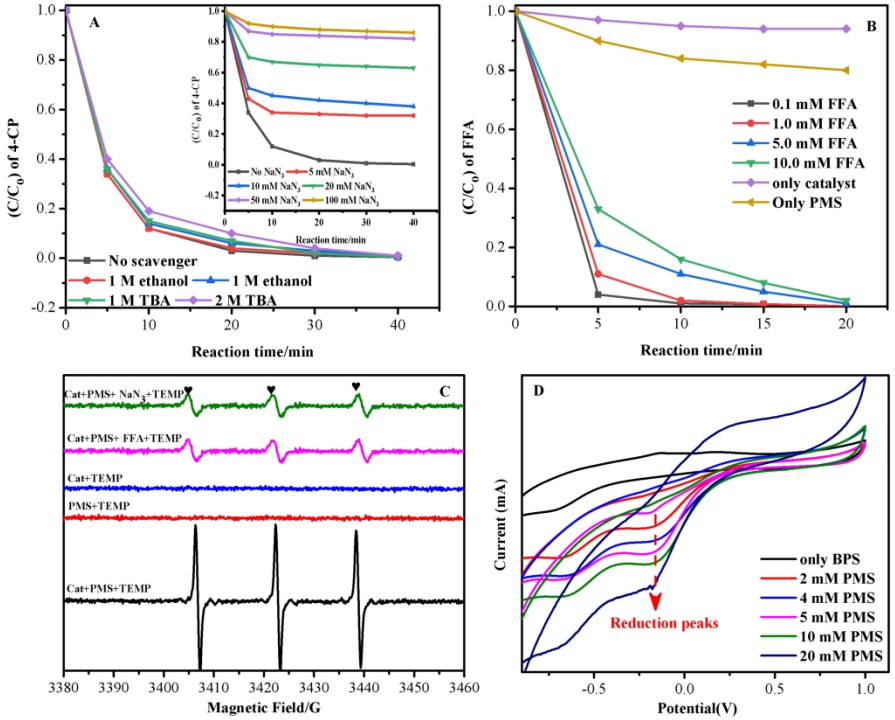

Fig. 2 (A) Influences of ethanol and TBA on the activity of CuOMgO/Fe3O4, (inset showing the influence of NaN3 on the activity of CuOMgO/Fe3O4 (B) degradation of FFA as 1O2- indicator (C) generation of 1O2 with TEMP (D) CV plots showing the increase in the reduction peak of CuOMgO/Fe3O4+PMS system with increasing PMS amount.
Conditions: 4-CP 40 ppm, PMS 2 mM, catalyst 0.2g/L, reaction temperature 30 oC and reaction time 40 min.

203x159mm (400 x 400 DPI)

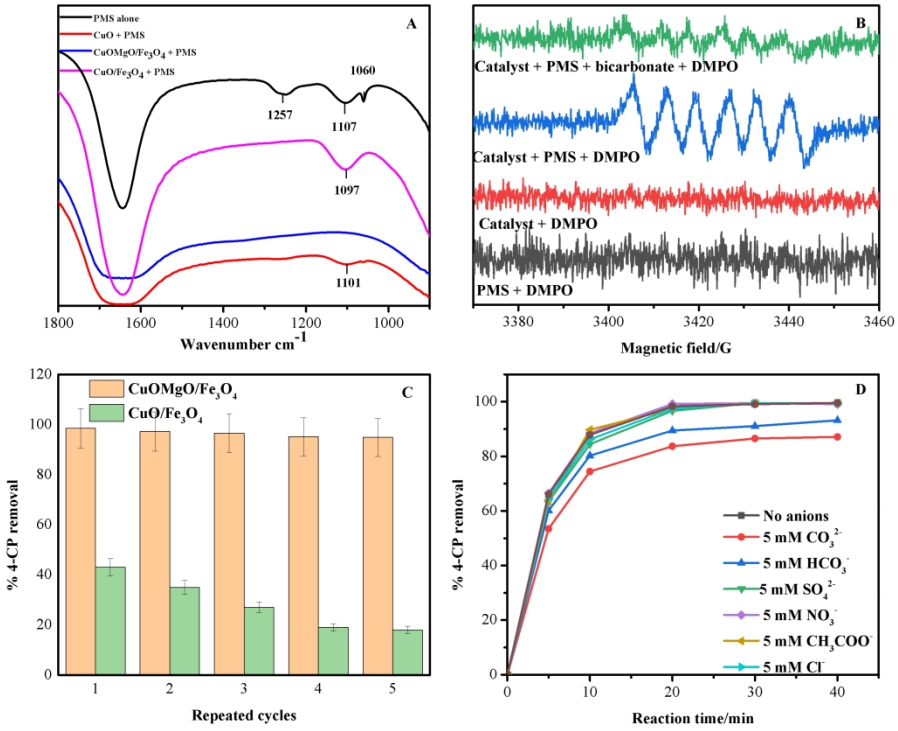

Fig. 3 (A) ATR-FTIR spectra of PMS after interacting CuOMgO/Fe3O4, CuO/Fe3O4 and CuO catalysts (B) generation of DMPO-O2 adduct in ethanol, giving strong evidence for the presence of super oxides in CuOMgO/Fe3O4+PMS system (C) stability of CuOMgO/Fe3O4, CuO/Fe3O4 in the recycled experiments (D) influence of anions on the catalytic activity of CuOMgO/Fe3O4+PMS system.

204x160mm (400 x 400 DPI)

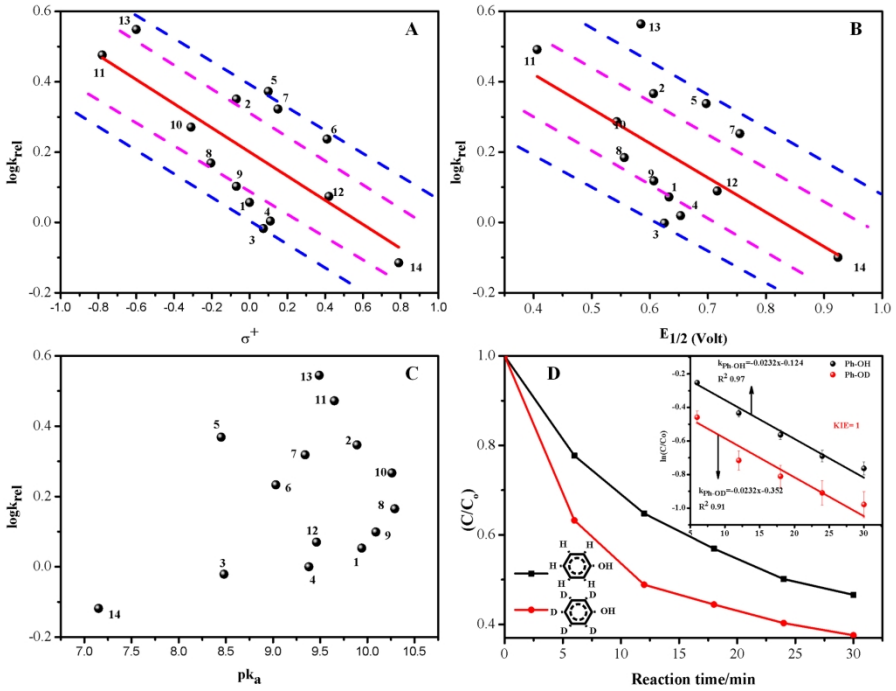

Figure 4 Quantitative structure-activity relationships of substituted phenols for (A) Hammett □+ constant, (B) half-wave potential (E1/2) (C) pKa and (D) Calculating KIE using CuOMgO/Fe3O4+PMS system.

221x163mm (300 x 300 DPI)